Proc. Natl. Acad. Sci. USA
Vol. 92, pp. 9843–9850, October 1995
Biophysics

Inaugural Article: This is the first contribution by Gregory A. Petsko, who was elected a Member of the National Academy of Sciences on April 25, 1995.

Structures of the apo- and the metal ion-activated forms of the diphtheria *tox* repressor from *Corynebacterium diphtheriae*

NIKOLAUS SCHIERING*†, XU TAO‡, HUIYAN ZENG‡, JOHN R. MURPHY‡, GREGORY A. PETSKO*, AND DAGMAR RINGE*§

*Departments of Chemistry and Biochemistry, and Rosenstiel Basic Medical Sciences Research Center, Brandeis University, Waltham, MA 02154; and ‡Section of Biomolecular Medicine, Boston University Medical Center Hospital, Boston, MA 02118

Contributed by Gregory A. Petsko, August 7, 1995

ABSTRACT **The diphtheria *tox* repressor (DtxR) of *Corynebacterium diphtheriae* plays a critical role in the regulation of diphtheria toxin expression and the control of other iron-sensitive genes. The crystal structures of apo-DtxR and of the metal ion-activated form of the repressor have been solved and used to identify motifs involved in DNA and metal ion binding. Residues involved in binding of the activated repressor to the diphtheria *tox* operator, glutamine 43, arginine 47, and arginine 50, were located and confirmed by site-directed mutagenesis. Previous biochemical and genetic data can be explained in terms of these structures. Conformational differences between apo- and Ni-DtxR are discussed with regard to the mechanism of action of this repressor.**

Iron is an essential nutrient for most living organisms and low levels of this element signal the expression of virulence determinants in many pathogenic microorganisms (1). It has been known for >50 years that the addition of iron to the growth medium of toxigenic *Corynebacterium diphtheriae* results in the inhibition of toxin production (2). Subsequently, it was found that diphtheria toxin is only expressed at maximal rates when iron becomes the growth rate-limiting substrate (3). The diphtheria toxin structural gene, *tox*, has been shown to be carried by a family of related corynebacteriophages (4). The regulation of *tox* expression, however, is mediated by the corynebacterial-determined repressor DtxR. *In vitro* studies have shown that DtxR is activated by divalent transition metal ions and, once activated, specifically binds to the diphtheria *tox* operator and other related palindromic DNA targets (5–9).

An understanding of the mechanism of interaction of the repressor with its cognate DNA requires knowledge of the three-dimensional structure of the repressor in its inactive and activated forms, as well as of its complex with DNA. The regulator of this interaction is an atom of iron, which binds to a specific site(s) on the repressor and causes a conformational change that is required for operator binding (10, 11). DtxR also regulates the transcription of other iron-sensitive genes in the same manner. Other divalent metal ions, especially nickel(II), can substitute for iron *in vitro*. This paper reports the crystal structure of apo-DtxR at 3-Å resolution and the preliminary structure of the nickel-bound holo-repressor.¶ Comparison of these structures, together with information from site-directed mutagenesis and other biochemical experiments, has allowed us to identify the activating metal-binding site and the region of the repressor that recognizes DNA. We propose a model for metal-dependent DNA binding.

Recently Qiu *et al.* (12) reported the structures of several metal-bound forms of DtxR at similar resolution. Our work presents the structure of the apo-repressor and a comparison between the inactive and activated forms. The activating metal site that we propose differs from that suggested by Qiu *et al.* (12).

MATERIALS AND METHODS

Crystallization and Data Collection. Recombinant DtxR was crystallized in space group $P3_221$ by vapor diffusion by employing the hanging drop method at room temperature using protein at a concentration of 15 mg/ml and 1.6 M ammonium sulfate/2% PEG 200/1 mM dithiothreitol/100 mM Hepes (pH 7.0) in the reservoir as described (13).

Soaking of crystals of apo-DtxR in mother liquor containing 0.1 mM $NiCl_2$ results in a change of space group to $P3_121$ and in the reduction of the length of the *c* axis by ≈50% (see Table 1). Using >0.5 mM $NiCl_2$ in soaking leads to cracking of the crystals.

Native, heavy atom derivative and Ni-DtxR data were collected on a Siemens X100 area detector mounted on an Elliot GX-6 rotating anode x-ray generator operated at 30 kV and 30 mA and evaluated with XDS (14).

Multiple Isomorphous Replacement (MIR) Analysis, Model Building, and Refinement. *Apo-DtxR.* Dimercury acetate (saturated, 18 h), ethyl mercury phosphate (1 mM, 18 h), and potassium mercury tetrathiocyanate (0.25 mM, 16 h) gave isomorphous heavy atom derivatives. Initial sites were established by deconvolution of difference Patterson maps with the aid of direct methods (15). Self- and cross-difference Fourier maps were used to locate additional sites which were confirmed in difference Patterson maps. The heavy atom positions were refined to a resolution of 3.5 Å (16). Six independent heavy atom positions in the three derivatives (*a, b, c* and *a′, b′, c′*) defined the orientation and position of the noncrystallographic molecular two-fold axis, which was refined to 179.6° by the program IMP of the RAVE package furnished by G. J. Kleywegt and T. A. Jones. Solvent flattening, two-fold iterative noncrystallographic symmetry averaging, and phase extension to 3-Å resolution were employed using the programs BCWANG (17), SQUASH (18), and RAVE and programs of the CCP4 package (19). The resulting electron density map showed a considerable improvement over the original MIR map and allowed tracing of a contiguous chain of 109 residues as polyalanine using the

Abbreviations: DtxR, diphtheria *tox* repressor; HTH, helix–turn–helix; CAP, catabolite gene activator protein.

†Present address: Pharmacia Societa per Azioni, Nerviano-Milan, Italy.

§To whom reprint requests should be addressed.

¶The atomic coordinates have been deposited in the Protein Data Bank, Chemistry Department, Brookhaven National Laboratory, Upton, NY 11973 (reference 1DPR).

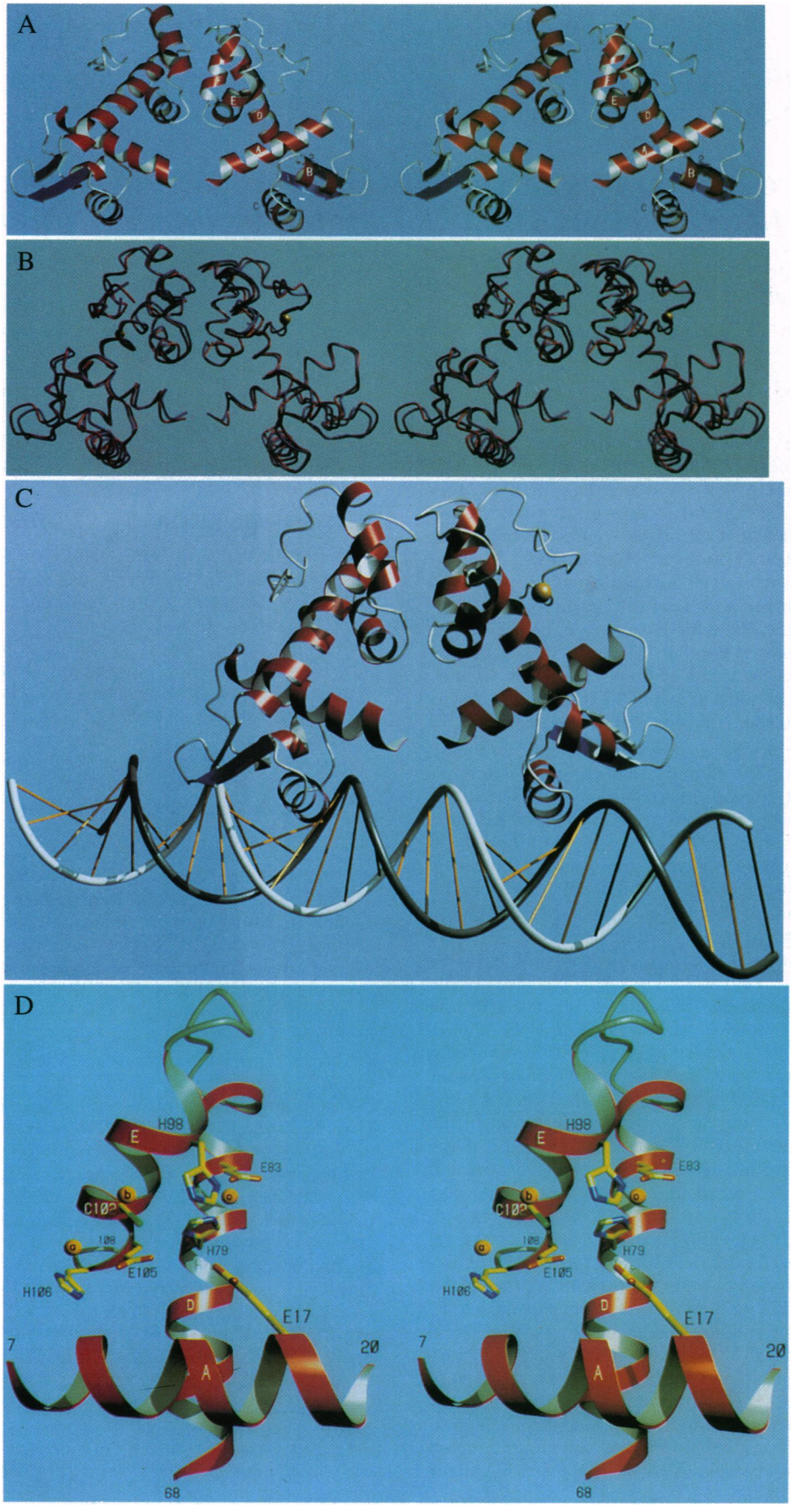

FIG. 1. (*Legend appears at the bottom of the opposite page.*)

Table 1. Data collection

Parameter	Native	DMA	EMP	PMT	Ni(II)
Unit cell, Å	$a = b = 64.0$, $c = 220.4$	$a = b = 64.4$, $c = 220.6$	$a = b = 64.2$ $c = 220.4$	$a = b = 64.5$ $c = 221.4$	$a = b = 64.9$ $c = 108.9$
Resolution, Å	3.0	3.5	3.5	3.5	3.8
Reflections					
Total	21,855	19,006	23,858	14,590	5,277
Unique	9,355	6,368	6,522	6,485	2,458
Completeness, %	83.8	84.9	85.6	83.2	86.2
R_{sym}, %	7.5	10.6	6.1	10.7	9.6
MFID		0.2	0.13	0.26	
Number of heavy atom sites		3	2	4	
F_H/E		1.3	1.5	1.5	
R_C		67.8	62.4	58.7	
$\langle m \rangle$	0.61				

DMA, dimercury acetate; EMP, ethyl mercury phosphate; PMT, potassium mercury tetrathiocyanate. Positions d coincide with positions a of the DMA derivative. $R_{sym} = \Sigma_h \Sigma_i |I_{h,i} - I_h| / \Sigma_h \Sigma_i I_{h,i}$, where $I_{h,i}$ are symmetry-related intensity observations and I_h is the mean intensity of reflexions with unique indices h. MFID (mean fractional isomorphous difference) $= \Sigma ||F_{PH}| - |F_P|| / \Sigma |F_P|$, where F_{PH} and F_P are the derivative and native structure factor amplitudes, respectively. $F_H/E = \sqrt{\Sigma f_H^2 / \Sigma (F_{PH,obs} - F_{PH,calc})^2}$. $R_C = \Sigma |F_{PH,obs} - F_{PH,calc}| / \Sigma |F_{PH,obs} - F_P|$ for centric reflections. $\langle m \rangle$ = Mean figure of merit including all three derivatives.

interactive model building program O (20). Additional improvement of the electron density map was achieved by combining the initial MIR phases and partial model information by using the program COMBINE (21). Several rounds of phase combination, positional refinement (22), initially by using noncrystallographic symmetry restraints, and manual rebuilding allowed the sequence to be assigned to the partial polyalanine chain and to include more residues at the C terminus. The positions of the heavy metals helped define the register of the polypeptide chain by identifying Cys-102, His-98, and His-79. The current model contains residues 3–136.

Beyond residue 136 two fragments of polyalanine containing a total of 46 residues could be built. The poor quality of the map in this region did allow neither assigning the connectivity of these fragments nor defining the relative alignment to the protein sequence, and including them into the phase combination procedure did not improve the quality of the resulting map. Furthermore, it appears that the conformation of this part is different for the two monomers in the asymmetric unit. Several attempts were undertaken to improve the interpretability of the electron density for the ill-defined C-terminal part of the structure, including the use of masks in averaging, different programs for solvent flattening, and phase extension without success. Therefore we conclude that this part of the structure is considerably flexible.

Ni-DtxR. One of the monomers of apo-DtxR was used as the starting model in the refinement of the structure of Ni-DtxR. First, rigid body refinement was employed followed by positional refinement using the program package X-PLOR (22). The position of the Ni ion could clearly be observed both in $F_o - F_c$ and $3F_o - 2F_c$ electron density maps. After manual rebuilding and inclusion of the Ni(II) into the coordinates, a second cycle of refinement was performed.

Ramachandran plots (23) for both monomers of apo-DtxR and for the Ni-DtxR monomer show only a few nonglycine residues lying outside the normally observed regions. An Eisenberg plot was created for apo-DtxR using a moving window of 21 residues (24). The profile score remained positive throughout the sequence corresponding to this structure, with an average score of 35.7. An estimate of the coordinate errors in the structures was obtained from a Luzzati plot (25). This analysis shows an estimated average coordinate error of 0.4 Å for both models.

Mutagenesis, Expression, and Purification of DtxR. The wt-DtxR and the mutants DtxR(Q43E), DtxR(R47H) (5), DtxR(R47D), DtxR(R50H), and DtxR(R50D) were purified from extracts of recombinant *Escherichia coli* and tested for DNA binding to a ^{32}P-labeled *C. diphtheriae tox* promotor/

FIG. 1 (*on opposite page*). (*A*) Stereo ribbon diagram of the N-terminal domains of the apo-DtxR dimer. The monomers have approximate dimensions of 32 Å × 40 Å × 25 Å. They are related by a noncrystallographic two-fold axis in the plane of the paper at a rotation of 179.6°. Residues exclusively from subdomain 2 form the metal ion activation site and yield the hydrophobic residues interacting in the dimer interface. (*B*) Stereo ribbon overlay of the apo- and Ni-DtxR dimers. Apo-DtxR is shown in red; Ni-DtxR is in blue. Also shown are the positions of Ni in the Ni-DtxR structure as yellow spheres. The two Ni sites are the pivot points around which each monomer rotates upon metal ion activation. The rotation axes are perpendicular to the plane of the page and the rotation leads to a closer approach of the two recognition helices at the bottom and to a further displacement of parts of the upper subdomain. (*C*) Model of the Ni-DtxR–DNA complex. A 30-mer of canonical B-form DNA was rendered in QUANTA (26). The position of the repressor with respect to the DNA was obtained by superimposing the Ni-DtxR dimer onto a model of the apo-DtxR–DNA complex. The latter was modeled using the structure of the catabolite gene activator protein (CAP)–DNA complex (27) in the following way. The HTH motif of one monomer of apo-DtxR was superimposed on one of the HTH motifs of CAP and the model DNA was superimposed accordingly. The second monomer was positioned as in the noncrystallographic dimer. The DNA in the CAP–DNA complex is curved. Since it is not known if DtxR induces DNA bending, we used straight DNA. Helix C of the other monomer of Ni-DtxR fits imperfectly into the neighboring major groove. The relatively short distance of about 31 Å between the two recognition helices in Ni-DtxR may indicate that a slight bending of the DNA occurs. The fit to Ni-DtxR would then be better. (*D*) Stereo drawing of the metal ion binding region of DtxR as identified by the binding sites for the mercury heavy atoms used to solve the crystal structure. Mercury site c corresponds to the Ni(II) binding site in our structure of Ni-DtxR and also to the metal ion binding site (site 1) identified as the activating metal ion site by Qiu *et al.* (12). Although mercury is an imperfect analog of a divalent transition metal ion, we believe that mercury site a is closer to the actual activating site for iron, which involves His-106, Glu-105, Cys-102, and possibly Glu-17. The images were generated using RAYSCRIPT (obtained from E. Fontana, D. Peisach, and E. Peisach, Brandeis University), a program that uses the input for MOLSCRIPT (28) to generate input for RAYSHADE (Version 4.0, written by Craig Kolb and Rod Bogart, Princeton University).

Table 2. Refined heavy atom positions

	Monomer 1			Monomer 2		
	x	*y*	*z*	*x*	*y*	*z*
DMA a	0.566	0.593	0.217	0.622	0.518	0.287
a′	0.492	0.603	0.206			
EMP b	0.495	0.596	0.205	0.612	0.449	0.296
PMT c	0.429	0.493	0.191	0.506	0.367	0.310
d	0.562	0.577	0.215	0.605	0.513	0.288

See legend to Table 1.

operator probe (3–5 fmol) by gel mobility shift as described (5). The mutants are 99% pure by SDS gel electrophoresis and immunoblot sensitive to the same extent as the wild-type protein using polyclonal antibodies raised against native DtxR.

RESULTS AND DISCUSSION

Three-Dimensional Structure. Apo-DtxR consists of 226 amino acid residues. The asymmetric unit of the crystal contains two monomers related by a noncrystallographic two-fold axis (Tables 1–3). Each monomer is composed of two domains, residues 1–136 and 137–226. In the electron density map only the N-terminal domain (residues 3–136) is clearly visible and of sufficient quality to position these residues. In contrast, the C-terminal domain is indicated only by fragmentary density of insufficient quality for continuous chain tracing, presumably due to considerable disorder in this part of the structure.

The N-terminal domain is mainly α-helical with a total of six helices and two β-strands (Fig. 1*A*). It is organized into two subdomains, 1 and 2, that are connected by a long α-helix [D (residues 66–88)]. Subdomain 1 is composed of three α-helices [*A* (residues 3–20), B (27–33), and C (38–50)] packed against two strands of antiparallel β-sheet [1 (53–57) and 2 (61–64)] and the N-terminal part of the connecting helix D. Subdomain 2 contains two α-helices [E (97–106) and F (110–119)] packed against opposite faces of the C-terminal portion of the connecting helix D. A helix–turn–helix (HTH) motif in subdomain 1 is formed by helices B and C (10).

Due to poor electron density only two fragments of the C-terminal domain containing a total of 46 residues could be modeled as polyalanine. They include one turn of an α-helix and three strands of a β-sheet. Since the connectivity within this motif and the nature of the side chains are ambiguous, this partial C-terminal domain is not included in the coordinates.

Table 3. Refinement

Parameter	Apo-DtxR	Ni-DtxR
Space group	$P3_221$	$P3_121$
Monomers/asymmetric unit	2	1
Resolution range, Å	8–3	8–3.8
No. of reflections $I/\sigma(I) > 2$	7378	1968
No. of protein atoms	2652	1327
R factor		
Cryst	23.3	19.3
Free	41.3	
B factor model	Group *B* factor	Group *B* factor
Deviation from ideal geometry (rmsd)		
Bond distances, Å	0.024	0.026
Bond angles, deg	4.8	4.8

$R_{cryst,free} = \Sigma||F_{obs}| - |F_{calc}||/\Sigma|F_{obs}|$, where the crystallographic and free *R* factors are calculated using either the working or free reflection set. The reflections for the latter set (8% of the total) were chosen before the start of the refinement and held separately since.

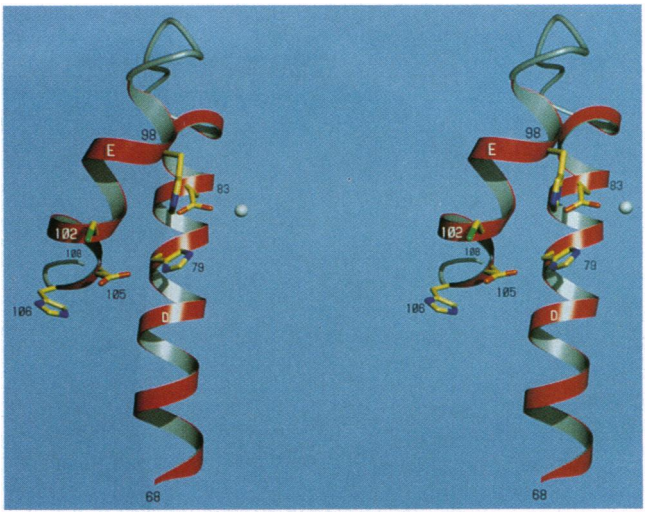

FIG. 2. Stereo representation of the Ni binding site observed when DtxR crystals are soaked in mother liquor containing 0.1 mM $NiCl_2$. Shown are Ni ligands His-79, Glu-83, and His-98 and the side chains of Cys-102, His-106, and Glu-105, along with the chain segment 68–108 (helices D and E). These latter three residues, together with Glu-17 (Fig. 1*D*), form putative metal ion-binding site 2, which we believe is required for full metal ion activation of DtxR binding to operator DNA. The role of Gln-130, which is described as an indirect ligand for site 1 via a water molecule by Qiu *et al.* (12), cannot be assessed by us as it is disordered in our electron density map. The image was rendered as described in the legend to Fig. 1.

The structure of the metal ion-activated form of DtxR was solved with data collected from a crystal of apo-DtxR after soaking it in mother liquor containing 0.1 mM $NiCl_2$. Binding of Ni(II) causes a reorientation of the monomers in the unit cell with the effect that the former noncrystallographic two-fold axis coincides with a crystallographic two-fold axis, and therefore a monomer now comprises the asymmetric unit. The orientations of the two-fold axes differ by 2° with a translation of about 2 Å at the centroid of the dimer.

A C^{α} ribbon diagram of Ni-DtxR is compared to that of apo-DtxR in Fig. 1*B* after superposition of the dimers. The rms deviation between C^{α} positions in the noncrystallographic apo-DtxR dimer and crystallographic Ni-DtxR dimer is 1 Å. The overall structures of the monomers are virtually identical, without significant changes in the internal relationship between the two subdomains (rms deviation between apo- and Ni-DtxR monomers: 0.83 and 0.95 Å, respectively). Additional electron density corresponding to Ni(II) is observed in subdomain 1 with residues from helices D and E being involved in Ni(II)-ligation as proposed previously (10) and as recently shown by Qiu *et al.* (12). This density is close enough to the side chains of residues His-79, Glu-83, and His-98 to identify these residues as ligands to the Ni(II) ion (Fig. 2). A positional difference of the monomers relative to each other can be observed in the dimer of Ni-DtxR compared to that of apo-DtxR. It can be ascribed to a rotary movement of each monomer by 2°, bringing subdomains 1 of the dimer closer while subdomains 2 diverge slightly. Because this movement is systematic, it is clearly detectable and different from the random changes in coordinates between the monomers of the apo- and Ni-DtxR structures. The pivot points for this movement are in subdomains 2 near His-79 and His-79′, and close to the Ni(II) ion binding sites.

DtxR has three major functions—DNA recognition, metal ion activation, and protein–protein interaction—the combination of which makes this protein unique among structurally characterized regulatory proteins to date. Furthermore, the results from mutagenesis experiments indicate that all of these functions reside in the N-terminal domain (9, 29, 30). Our

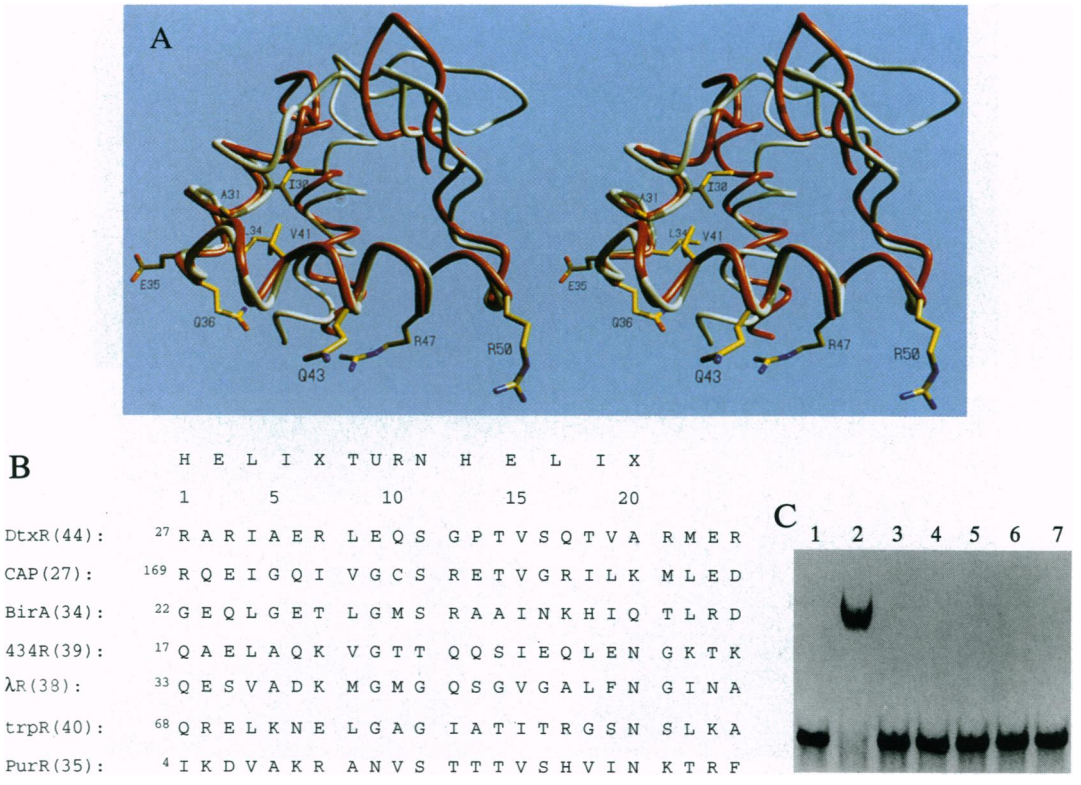

FIG. 3. Structural and sequence comparisons of HTH motifs. (*A*) Comparison of the HTH motifs of apo-DtxR and CAP (27). Shown in stereo are helices A, B, and C and strands 1 and 2 of DtxR (subdomain 1 in red) and the equivalent parts of CAP (in white). The superposition was performed with the command LSQ_EXPLICIT of the program O (20) using the C^{α} positions of residues 27–47 of DtxR and the corresponding C^{α} positions of CAP (169–189) and resulting in an rms deviation of 0.64 Å for this segment. Also shown are the DtxR side chains at position 30, 31, 34–36, and 41 of the HTH motif, which have implications in the folding and stability of this motif (32), and DtxR residues Gln-43, Arg-47, and Arg-50 in the recognition helix, which are implicated in DNA binding. The major topological difference of this part of CAP and DtxR is the presence of an additional β-hairpin between the first represented helix and the HTH motif in CAP forming a four-stranded sheet with the second β-hairpin. In DtxR there is a direct loop between helices A and B. This figure was generated as described in the legend to Fig. 1. (*B*) Sequence alignment for some HTH motifs. DtxR, diphtheria *tox* repressor; BirA, biotin operon repressor; 434R, 434 repressor; λR, λ repressor; trpR, *trp* repressor; PurR, purine repressor. The numbers in parentheses are references. (*C*) Gel electrophoresis mobility shift analysis of wild-type DtxR and DNA binding defective variants. Lanes: 1, −DtxR; 2, DtxR; 3, DtxR(Q43E); 4, DtxR(R47H); 5, DtxR(R47D); 6, DtxR(R50H); 7, DtxR(R50D). Mutation of positions predicted by the crystal structures to be involved in DNA recognition leads to loss of operator DNA binding.

structures of DtxR confirm these results and allow us to localize the exact sites at which each of these functions occur.

HTH Motif. A classical structural element that is associated with DNA recognition and binding is the HTH motif (31). The HTH motif consists of a core of 20 residues and is found in many prokaryotic regulatory proteins as well as in eukaryotic homeodomains (33). Among reported structures this motif is structurally nearly invariant. In the structures of apo- and Ni-DtxR it is formed by helices B and C (residues 27–50) of subdomain 1. Superposition of the C^{α} atoms of the HTH motif of apo-DtxR on the corresponding atoms of the CAP (27) yields an rms deviation of 0.64 Å (Fig. 3*A*). The same C^{α} positions of DtxR superimpose with an rms deviation of 0.8 Å on the corresponding C^{α} atoms of the biotin operon repressor BirA (34). In both instances the structural similarity extends beyond the HTH motif in both N- and C-terminal directions.

The strong structural conservation is not reflected in a correspondingly high degree of sequence similarity (Fig. 3*B*). For instance the sequence identity for the HTH motif of DtxR is only 25% with CAP and 15% with BirA. Comparisons of a number of protein sequences known or assumed to contain the HTH motif have been used by Brennan and Matthews (32) to describe the dominant characteristics for some key positions within the motif. These characteristics include a strong preference for apolar residues in positions 4, 8, 10, and 15 and for a glycine residue in position 9 [motif numbering convention of Pabo and Sauer (31)]. These residues in DtxR (30, 34–36, and 41) are shown in Fig. 3*A*. The "nonvariant" glycine is in the turn of the motif and adopts a left-handed α-helical backbone conformation that would be uncommon for nonglycine residues.

While apolar and unbranched residues are observed at the expected positions in the HTH motif of DtxR, a glutamate residue, Glu-35, is found at position 9. Thus, DtxR is the second example of a structurally characterized prokaryotic protein with a nonglycine residue at this position in the HTH motif. In the crystal structure of the purine repressor, PurR, an asparagine residue is found at the corresponding position (35). In addition, a functional point mutant of the λ repressor with a glutamate in place of the glycine in position 9 has been described (36), and nonglycine residues are not uncommon at this position in homeodomain proteins. For example, in the NMR derived structure of the *Drosophila* homeodomain protein antennapedia, a cysteine is found in the corresponding position (37).

DNA Recognition. Results from glutaraldehyde crosslinking and inactivation studies of apo-DtxR by apo-DtxR(Δ1–47), as well as the observed cooperativity in metal ion binding, suggest that the active form of DtxR is a dimer (30) (Fig. 1*A*) and that one activating metal ion binds per monomer (9, 30). DtxR(Δ1–47) is an in-frame mutant in which the HTH segment is deleted. Site-directed mutational analysis of residues in helix

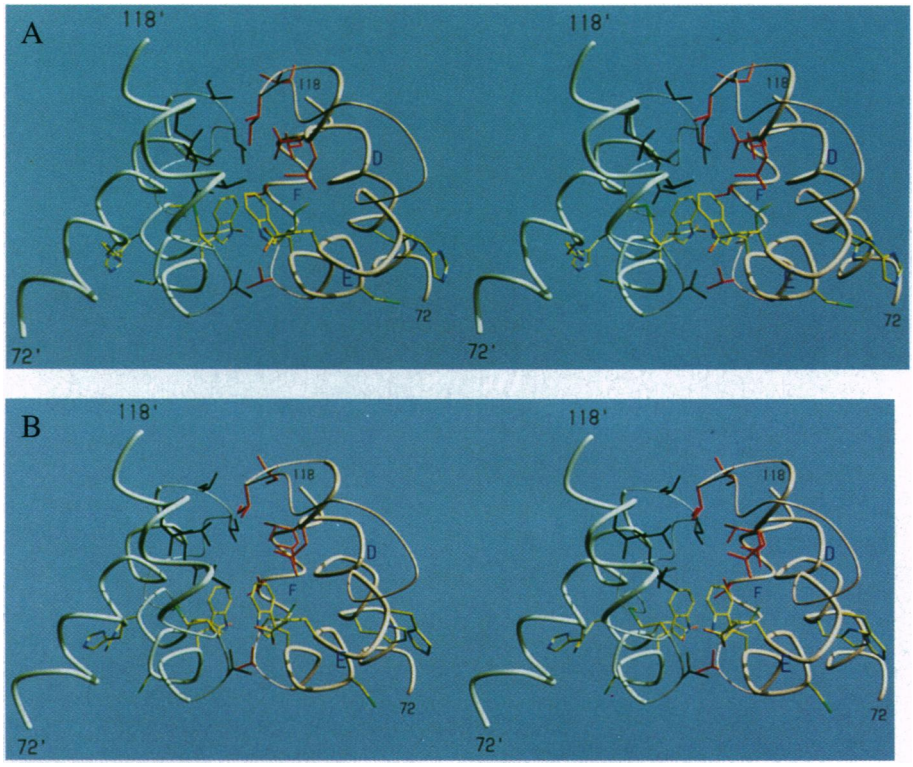

FIG. 4. Stereo images of the apo- (*A*) and Ni-DtxR (*B*) dimer interfaces showing the protein–protein interactions. Shown are helices D, E, and F (residues 72–118) of each of the two DtxR monomers. The backbone of one monomer is in white; the other is in pink. Aliphatic side chains are shown in black or red and all others are according to atom type. His-79, His-98, and Cys-102 are included for orientation to the metal binding site. Subtle differences in environment of the Trp-104 side chain could account for the fluorescence quenching observed when activating metal ions bind. This figure was generated as described in the legend to Fig. 1.

C of subdomain 1 supports the hypothesis that this portion of the HTH motif is the recognition element that interacts with DNA in the major groove (Fig. 3*C*). The two monomers in the asymmetric unit of the apo-DtxR crystal are arranged such that α-helices C and C′ of the dimer are approximately parallel to each other at a distance of about 32 Å with a dihedral angle of approximately 22° along the helix axes. Due to the rearrangement of the monomers in the dimer relative to each other, the distance between the recognition helices is shortened in the metal ion-activated form of the repressor by about 1 Å. One can model the interaction of DtxR with the DNA based on this distance and by analogy to other protein–operator complexes that have been structurally characterized (Fig. 1*C*). These include the phage repressors of λ and 434 and the *E. coli* trp repressor, CAP, and purine repressor (PurR) (35, 38–41). In each case, the second helix of the HTH motif, the recognition helix, interacts intimately with the major groove of DNA. However, the details of the interaction, the relative orientation of the recognition helix with respect to the major groove of DNA, as well as the conformation of the DNA itself differ, and no simple code relating protein sequences and DNA base sequences has been observed thus far. For instance, the repressors from the λ and 434 phages and CAP use either glutamine and/or arginine residues in the recognition helix to form bidentate or monodentate hydrogen bonds to adenine, guanine, or thymine bases in the major groove of DNA. In the recognition helix of DtxR there is one glutamine (Gln-43) residue and two arginine residues (Arg-47 and Arg-50), all of which point in the direction where DNA interaction has to be assumed, suggesting to us that these residues might play a direct role in DNA recognition. An involvement of Gln-43 is also supported by its alignment with Gln-33 in a comparison of the sequences and structures of DtxR and the phage 434 repressor. Gln-33 of the phage 434 repressor forms a hydrogen bond to a thymine in the DNA complex (39).

We therefore used site-directed mutagenesis to introduce Q43E, R47D, R50H, and R50D substitutions. These mutations as well as the nitrosoguanidine-induced R47H mutation result in a loss of binding to the ^{32}P-labeled *C. diphtheriae tox* promotor/operator (*toxPO*) probe (Fig. 3*C*). In addition, each of these DtxR mutants fails to regulate the expression of β-galactosidase from a *toxPO/lacZ* transcriptional fusion in recombinant *E. coli* (data not shown).

Most prokaryotic repressors use residues in the first turn of the second α-helix of their HTH motif [helixC in this structure (10)] for sequence-specific DNA interaction (31). It is interesting to note that the residues found to be involved in DNA recognition, Gln-43, Arg-47, and Arg-50, are in the second through fourth turn of this helix. This observation leads to a model of DNA recognition similar to that of eukaryotic homeodomains (31).

Metal Ion Binding Domain. In the apo-DtxR structure, the three unique mercury positions of the heavy atom derivatives for each monomer cluster around a region in the second subdomain within 3.4 Å of the side chains of His-79, Glu-83, His-98, Cys-102, Glu-105, and His-106 and within 5.5 Å of Glu-17. The location of these mercury sites led us to originally propose this region as the metal ion binding domain (10).

Recently Qiu *et al.* (12) have reported the three-dimensional structures of DtxR in complex with divalent transition metal ions at 2.8-Å resolution. In those cocrystal structures a considerable part of the C-terminal domain of DtxR also could not be modeled. Upon soaking of apo-DtxR crystals in mother liquor containing $NiCl_2$ we observe that the space group and unit cell parameters change to the same values as found for the cocrystal structures with Fe, Cd, Mn, Zn, and Co presented by Qiu *et al.* (12). Surprisingly, the unit cell of Ni-DtxR reported by these authors is slightly different with the *c* axis being shortened by about 4 Å compared to all other cocrystals and to the soaked Ni-DtxR structure presented here.

Qiu *et al.* (12) have reported two distinct metal ion binding sites: Site 1 is observed in the presence of the activating metal ions Fe^{2+}, Mn^{2+}, Co^{2+}, Zn^{2+}, and Ni^{2+}, which form a complex with His-79, Glu-83, His-98, and a water molecule as a fourth ligand. Cd^{2+} binds to site 1 and also to a lower-affinity site, site 2, which is formed by the side chains of Glu-105, His-106, the carbonyl oxygen of Cys-102, and a solvent molecule. The site occupied by Ni(II) in our Ni-DtxR structure corresponds to site 1 (Fig. 2). Qiu *et al.* also ascribe a role to Gln-130 as an indirect ligand for the metal ion at site 1 through a water molecule. This residue is disordered in the Ni-DtxR structure presented here.

In the apo DtxR structure presented here, the same metal ion binding region was identified based on the mercury positions of the heavy atom derivatives. Mercury position a (Fig. 1*D*) corresponds to site 2 in the cocrystal structure reported by Qiu *et al.* (12), whereas position c corresponds to site 1. The involvement of some of these residues in metal ion binding by DtxR has been deduced previously (10). In addition, the arrangement of a histidine and cysteine separated by one turn in a helix (such as His-106 and Cys-102) has been shown to form a high-affinity metal chelating site in other proteins (42). Results from mutagenesis experiments suggest that at least His-106 and Cys-102 of DtxR are involved in metal ion activation. For instance, the metal ion-binding defective mutant H106Y has been shown to have reduced repressor activity as measured by β-galactosidase expression from a small *toxPO/lacZ* transcriptional fusion and by gel retardation assays (9). Cys-102 has been replaced by all other amino acid residues; however, only an aspartate in this position results in active metal-ion-dependent variant of the repressor (7). These results, together with our observation that metal ions can bind in more than one site on DtxR, would argue that the activating iron binding site is closer to mercury position a (Fig. 1*D*) and includes the side chains of His-106, Glu-105, Cys-102, and possibly Glu-17 (Fig. 3). Soaking our DtxR crystals in mother liquor containing high concentrations of activating transition metal ions [Ni(II), Cd(II), Mn(II)] results in cracking, suggesting conformational changes upon metal ion binding at additional sites. The failure of Qiu *et al.* (12) to identify what we believe is the activating metal ion site in their cocrystallization experiments may be due to inhibitory effects of the crystal mother liquor, oxidation of Cys-102, and/or the necessity for DNA to be bound in order for this site to be utilized.

How Does Metal Ion Binding Activate the Repressor? The distance between adjacent major grooves of canonical B-form DNA is 34 Å. In the apo-DtxR structure the distance between the C^{α} positions of Gln-43 in helices C and C′ is about 32 Å, whereas in the Ni-activated form of the repressor reported here, the corresponding distance is shorter by about 1 Å and in accordance with the distance of 30 Å reported by Qiu *et al.* (12). This relatively short distance suggests that the DNA may be bent in the repressor–operator complex. The movement of the recognition helices toward each other is due to a reorientation of the monomers relative to each other. This is accomplished by a rotation of each monomer by 2° with the rotation centers being close to the metal ion binding sites.

That type of switching mechanism leads to a model for metal ion-dependent DNA binding, in which the N-terminal domains act like a caliper with the metal atoms functioning as the pins at the pivot points.

If our hypothesis, that the activating metal ion site is formed by His-106, Glu-105, Cys-102, and possibly Glu-17, is correct, then the changes described above may not represent the full extent of the activating conformational changes induced by metal ion binding. However, since binding of an activating metal ion at one site is capable of producing a conformational change in the relative orientation of subdomains, this general mechanism of activation is certainly possible for DtxR. Glu-17 of DtxR provides a potential direct bridge between the metal ion binding region and the HTH motif. This residue is located in helix A. On ligation to an activating metal ion in site 2, movement of the side chain of Glu-17 could drag helix A and the HTH motif further than observed when Ni(II) binds to site 1. This movement would change the distance between the recognition helices even more than the 2-Å change seen in our structure comparison.

Protein–Protein Interaction at the Dimer Interface. In the apo-DtxR structure we observe a dimer in the asymmetric unit. There is considerable evidence from solution studies that the metal ion-activated form of DtxR that binds DNA is at least a dimeric complex (30). The interface between the two monomers is comprised of a tight hydrophobic network formed by residues of subdomains 2 (Fig. 4). The residues involved in protein–protein interaction originate from helices D, E, and F and loops D–E and E–F. The residues forming the hydrophobic interface are Leu-85, Leu-86, Ile-89, Ile-90, Trp-104, Val-107, Met-108, Val-112, and Leu-116. Leu-85, Ile-89, Trp-104, and Val-107 are in van der Waals contact to their symmetry mates from the other monomer. The only polar residue at the interface is Glu-100, which forms an internal hydrogen bond to Trp-104. The two previously described mutants, E100K and W104Q, were found to have markedly decreased repressor activity as measured by β-galactosidase expression from a *toxPO/lacZ* transcriptional fusion (9). Trp-104 has a prominent position at the center of this hydrophobic core. In the Ni-DtxR structure this interface is formed by monomers related by a crystallographic two-fold axis (Fig. 4). Upon addition of activating metal ions, quenching of the intrinsic tryptophane fluorescence is observed (30). Subtle differences in the environment of the Trp-104 residues in the apo- and Ni-DtxR structures could account for the observed fluorescence quenching. The emission wavelength of 333 nm suggests that the indole ring of tryptophane is buried within the protein (data not shown) as confirmed by our crystal structures of apo- and Ni-DtxR.

CONCLUSIONS

Comparison of the structures of apo- and Ni-DtxR leads to a caliper model for metal ion activation. Binding of Ni(II) or Fe(II) causes a conformational change in the relative orientation of the monomers in the dimeric structure, changing the distance between the recognition helices of the HTH motifs. It is not known if the operator DNA undergoes a conformational change when DtxR binds. The relatively short distance between the recognition helices observed here supports the hypothesis that the DNA may be slightly bent in the DtxR–DNA complex. The actual conformation of DtxR may also change more dramatically upon interaction with operator DNA and upon binding of a metal ion to the site formed by His-106, Glu-105, Cys-102, and possibly Glu-17. This caliper model for ligand-activated DNA binding may explain how other metal ion-dependent DNA binding proteins such as MerR may function (43). Structural studies of the DtxR–DNA complex with all metal sites occupied will be needed to validate this model and to provide insights into possible roles for the disordered C-terminal domain.

We thank Daniel and Ezra Peisach and Drs. Marty Stanton and David Harrison. This work was supported by a fellowship of the Wissenschaftsausschuss der North Atlantic Treaty Organization über den Deutscher Akademischer Austauschdienst (N.S.), by a grant from the National Institutes of Health (J.R.M. and D.R.), and (in part) by a grant from the Lucille P. Markey Charitable Trust (D.R.).

1. Litwin, C. M. & Calderwood, S. B. (1993) *Clin. Microbiol. Rev.* **6,** 137–149.
2. Pappenheimer, A. M., Jr., & Johnson, S. J. (1936) *Br. J. Exp. Pathol.* **17,** 335–341.

3. Pappenheimer, A. M., Jr. (1955) *Symp. Soc. Gen. Microbiol.* **5,** 40–56.
4. Buck, G. A., Gross, R. E., Wong, T. P., Lorea, T. & Groman, N. B. (1985) *Infect. Immun.* **49,** 679–684.
5. Tao, X., Boyd, J. & Murphy, J. R. (1992) *Proc. Natl. Acad. Sci. USA* **89,** 5897–5901.
6. Tao, X. & Murphy, J. R. (1992) *J. Biol. Chem.* **267,** 21761–21764.
7. Tao, X. & Murphy, J. R. (1994) *Proc. Natl. Acad. Sci. USA* **91,** 9646–9650.
8. Schmitt, M. P. & Holmes, R. K. (1993) *Mol. Microbiol.* **9,** 173–181.
9. Wang, Z., Schmitt, M. P. & Holmes, R. K. (1994) *Infect. Immun.* **62,** 1600–1608.
10. Tao, X., Schiering, N., Zeng, H., Ringe, D. & Murphy, J. R. (1994) *Mol. Microbiol.* **14,** 191–197.
11. Schmitt, M. P. & Holmes, R. K. (1991) *Infect. Immun.* **59,** 1899–1904.
12. Qiu, X., Verlinde, C. L. M. J., Zhang, S., Schmitt, M. P., Holmes, R. K. & Hol, W. G. J. (1995) *Structure* **3,** 87–100.
13. Schiering, N., Tao, X., Murphy, J. R., Petsko, G. A. & Ringe, D. (1994) *J. Mol. Biol.* **244,** 654–656.
14. Kabsch, W. (1988) *J. Appl. Crystallogr.* **21,** 916–924.
15. Sheldrick, G. M. (1995) in *Crystallographic Computing* (Oxford Univ. Press, Oxford), Vol. 3, p. 175.
16. Dickerson, R. E., Weinzierl, J. E. & Palmer, R. A. (1968) *Acta Crystallogr. Sect. B* **24,** 997–1003.
17. Wang, B. C. (1985) *Methods Enzymol.* **115,** 90–112.
18. Zhang, K. Y. (1993) *Acta Crystallogr. Sect. D* **49,** 213–222.
19. Science and Engineering Research Council (1979) CCP4, Collaborative Computing Project No. 4 (Daresbury Lab., Warrington, U.K.).
20. Jones, T. A., Zou, J. Y., Cowan, S. W. & Kjeldgaard, M. (1991) *Acta Crystallogr. Sect. A* **47,** 110–119.
21. Kabsch, W., Mannherz, H. G., Suck, D., Pai, E. F. & Holmes, K. C. (1990) *Nature (London)* **347,** 37–44.
22. Brünger, A. T. (1992) X-PLOR, A System for X-Ray Crystallography and NMR (Yale Univ. Press, New Haven, CT), Version 3.1.
23. Ramachandran, G. N. (1968) *Adv. Protein Chem.* **28,** 283–437.
24. Bowie, J. U., Lüthy, R. & Eisenberg, D. (1991) *Science* **253,** 164–170.
25. Luzzati, P. V. (1952) *Acta Crystallogr.* **5,** 802–810.
26. Molecular Stimulations (1994) QUANTA 4.0 (Molecular Simulations, Burlington, MA), Version 4.0.
27. McKay, D. B. & Steitz, T. A. (1981) *Nature (London)* **290,** 744–749.
28. Kraulis, P. J. (1991) *J. Appl. Crystallogr.* **24,** 946–950.
29. Tao, X. & Murphy, J. R. (1993) *Proc. Natl. Acad. Sci. USA* **90,** 8524–8528.
30. Tao, X., Zeng, H.-y. & Murphy, J. R. (1995) *Proc. Natl. Acad. Sci. USA* **92,** 6803–6807.
31. Pabo, C. O. & Sauer, R. T. (1984) *Annu. Rev. Biochem.* **53,** 293–321.
32. Brennan, R. G. & Matthews, B. W. (1989) *J. Biol. Chem.* **264,** 1903–1906.
33. Harrison, S. C. (1991) *Nature (London)* **353,** 715–719.
34. Wilson, K. P., Shewchuk, L. M., Brennan, R. G., Otsuka, A. J. & Matthews, B. W. (1992) *Proc. Natl. Acad. Sci. USA* **89,** 9257–9261.
35. Schumacher, M. A., Choi, K. Y., Zalkin, H. & Brennan, R. G. (1994) *Science* **266,** 763–770.
36. Hochschild, A., Irwin, N. & Ptashne, M. (1983) *Cell* **32,** 319–325.
37. Quian, Y. Q., Billeter, M., Otting, G., Müller, M., Gehring, W. J. & Wüthrich, K. (1989) *Cell* **59,** 573–580.
38. Jordan, S. R. & Pabo, C. O. (1988) *Science* **242,** 893–899.
39. Aggarwal, A. K., Rodgers, D. W., Drottar, M., Ptashne, M. & Harrison, S. C. (1988) *Science* **242,** 899–907.
40. Otwinowski, Z., Schevitz, R. W., Zhang, R.-G., Lawson, C. L., Joachimiak, A., Marmorstein, R. Q., Luisi, B. F. & Sigler, P. B. (1988) *Nature (London)* **335,** 321–329.
41. Schultz, S. C., Shields, G. C. & Steitz, T. A. (1991) *Science* **253,** 1001–1007.
42. Arnold, F. H. & Haymore, B. L. (1991) *Science* **252,** 1796–1797.
43. O'Halloran, T. V. (1993) *Science* **261,** 715–725.
44. Boyd, J. M., Hall, K. C. & Murphy, J. R. (1992) *J. Bacteriol.* **174,** 1268–1272.